

On Impact of Helical Structures on Stabilization of Swirling Flames with Vortex Breakdown

Dulin, V. M.; Lobasov, A. S.; Chikishev, L. M.; Markovich, D. M.; Hanjalic, K.

DOI

[10.1007/s10494-019-00063-7](https://doi.org/10.1007/s10494-019-00063-7)

Publication date

2019

Document Version

Accepted author manuscript

Published in

Flow, Turbulence and Combustion

Citation (APA)

Dulin, V. M., Lobasov, A. S., Chikishev, L. M., Markovich, D. M., & Hanjalic, K. (2019). On Impact of Helical Structures on Stabilization of Swirling Flames with Vortex Breakdown. *Flow, Turbulence and Combustion*, 103(4), 887-911. <https://doi.org/10.1007/s10494-019-00063-7>

Important note

To cite this publication, please use the final published version (if applicable). Please check the document version above.

Copyright

Other than for strictly personal use, it is not permitted to download, forward or distribute the text or part of it, without the consent of the author(s) and/or copyright holder(s), unless the work is under an open content license such as Creative Commons.

Takedown policy

Please contact us and provide details if you believe this document breaches copyrights. We will remove access to the work immediately and investigate your claim.

On impact of helical structures on stabilization of swirling flames with vortex breakdown

V.M. Dulin^{1,2}, A.S. Lobasov^{1,2}, L.M. Chikishev^{1,2}, D.M. Markovich^{1,2},
K. Hanjalic³

¹*Kutateladze Institute of Thermophysics, 1 Lavrentyev Avenue, Novosibirsk, 630090, Russia*

²*Novosibirsk State University, 2 Pirogov Street, Novosibirsk, 630090, Russia*

³*Chemical Engineering Department, Delft University of Technology, 58, Van der Maasweg 9, Delft, The Netherlands*

phone: +7 383 335 66 84

vmd@itp.nsc.ru

Abstract We report on a study of the impact of coherent helical vortex structures on the shape of the reaction zone and heat release in swirling methane/air flames in regimes with a vortex breakdown. Three kinds of atmospheric flames are considered, viz., fuel-lean and fuel-rich premixed flames and a partially premixed fuel-rich lifted flame. Based on the measurements of the velocity fields by a stereo PIV in combination with the OH PLIF and HCHO PLIF, the impact of the coherent flow structures on large-scale corrugations of the reaction zone is evaluated. Helical vortex structures, detected in both the non-reacting and reacting high-swirl flows by using proper orthogonal decomposition, are found to promote combustion both in the lean premixed and fuel-rich partially premixed flames. In the first case, based on the phase-averaged intensity of the HCHO×OH signal and the location of the helical vortex structure in the inner mixing layer, it is concluded that the vortex locally increases the heat release rate by enlarging the flame front and enhancing the mass exchange between the combustion products inside the recirculation zone and the fresh gases. The events of the local flame extinctions are detected in the instantaneous PLIF snapshots for the lean mixture, but they do not cause extinction of the entire flame or a blow-off. In case of the lifted flame, the outer helical vortex structure promotes combustion by locally intensifying the mass exchange between the fuel-rich jet with the surrounding air.

Keywords: swirling flame, coherent structures, precessing vortex core, vortex breakdown, stereo PIV, OH PLIF, HCHO PLIF, conditional sampling

Abbreviations

CCD: charge-coupled device;

CH PLIF: methylidyne planar laser-induced fluorescence;

FWHM: full width at half maximum;

HCHO PLIF: formaldehyde planar laser-induced fluorescence;

LDA: laser Doppler anemometer;

LES: large eddy simulation;

OH PLIF: hydroxyl planar laser-induced fluorescence;

PIV: particle image velocimetry;

PLIF: planar laser-induced fluorescence;

POD: proper orthogonal decomposition;

PVC: precessing vortex core;

YAG: Yttrium aluminium garnet.

1 Introduction

Swirling motion is often imposed on the flow inside burners, combustion chambers and furnaces to ensure stable combustion in the compact zone. This is usually achieved in a low-velocity region and is formed in the core of the swirling flow after passing through an expansion [1-3]. When the swirl is strong enough, the vortex core undergoes a breakdown, resulting in the formation of a low-pressure wake and an abrupt change of the flow pattern [4-8]. A further increase in the swirl strength causes local flow recirculation inside the wake. During combustion, hot products concentrate in the low-pressure region of the vortex core and become trapped within the recirculation zone [9-12]. Thereby, the heat and mass exchange between the fresh mixture issuing from the swirler and gases inside the recirculation zone provides favourable conditions for the successful ignition of the flame and stable combustion [13,14]. Cheng et al. (e.g., [15-17]) reported achieving a stable flame for a low-swirl burner without a central recirculation zone. The flame stabilization was provided by a low-velocity wake produced by a swirler with a perforated centre-body. The absence of the central recirculation zone and a short residence time for such burner geometry resulted in a decrease in the NO_x concentration in the combustion products for fuel-lean mixtures. This context emphasizes the importance of aerodynamics optimization when designing swirl burners.

Another phenomenon in swirling flows is a precession of the vortex core [4,5,18]. In some cases, the precessing is weak, whereas in others, it is coupled with strong velocity and pressure fluctuations [7,19-27]. The phenomenon of the precessing vortex core (PVC) has been studied extensively for different swirling flow

configurations, including swirling jets. Based on laser Doppler anemometry (LDA) measurements in a turbulent swirling jet, Cala et al. [28] averaged the local velocity with respect to the phase of the quasi-periodic pressure fluctuations monitored by a pressure probe placed near the nozzle exit. By assuming that the pressure oscillations were induced by a rotating coherent structure, the authors reconstructed a 3D shape of the structure. It was found to consist of a PVC and two secondary helical vortices. One secondary vortex was induced in the inner mixing layer around the central recirculation zone, whereas the other was found in the outer mixing layer.

Similar coherent structures were later detected in other studies of swirling jets with a vortex breakdown using pointwise LDA and planar particle image velocimetry (PIV) measurements [29-31]. Oberleithner et al. [29] phase-averaged the velocity fields measured in a high-swirl jet with a vortex breakdown by PIV by using a snapshot method for proper orthogonal decomposition (POD) [32]. The observed coherent structure consisted of PVC, spiralling inside the central recirculation zone, and a secondary helical vortex in the outer mixing layer. Later, based on the direct measurements of 3D velocity fields by tomographic PIV and POD processing, Alekseenko et al. [33] verified the assumption that quasi-periodic velocity and pressure fluctuations were caused by the rotation of the coherent structure. This assumption was used in previous studies for deducing the 3D field from the 2D PIV data [29,30]. Alekseenko et al. proved that the winding direction of the outer helical vortex was opposite that of the jet swirl. Additionally, the presence of the outer helical vortex in the instantaneous 3D velocity fields could be observed in tomographic PIV measurements in [34] and [35].

However, the specific impacts of such large-scale helical vortex structures, including the PVC on the stabilization of flames, unsteady combustion and thermoacoustic pulsations, are not completely understood [18, 36-38]. Based on LDA measurements of the flow in a swirl burner with and without premixed combustion, Schneider et al. [39] reported clear evidence that the PVC could be found only in the latter case. In contrast, Anacleto et al. [10] found that the intensity of quasiperiodic pressure fluctuations, produced by the PVC of the flow in model combustion chambers with a breakdown of the vortex core and the central recirculation zone, was not strongly altered during lean premixed combustion. Later, based on a large eddy simulation (LES) of the reacting flow for the same

geometry, Duwig and Fuchs [40] demonstrated that the PVC movement was statistically correlated with a local variation in the density, indicating that the coherent flow structure affected the unsteady dynamics of flame and local heat release.

In their LDA measurements of flow in a non-premixed fuel-lean model gas turbine combustor, Janus et al. [41] observed that the PVC was present in both non-reacting and reacting flow configurations. Alekseenko et al. [30] demonstrated that a lifted fuel-rich propane flame does not significantly alter the shape of the coherent structure, which consists of PVC and a secondary helical vortex, in a swirling jet with a vortex breakdown. It was also demonstrated that modulation of the jet flow rate could be used for intensifying the jet mixing with the surrounding air via forced formation of the toroidal vortices and increasing the combustion efficiency near the burner outlet. Based on a linear hydrodynamics stability analysis, Terhaar et al. [42] found that the velocity and density distributions inside the recirculation zone strongly affect the amplitude of the PVC. In another paper, Terhaar et al. [25] demonstrated that the axial injection of an additional jet resulted in a modification of the recirculation zone and was efficient for the suppression of the PVC amplitude.

It has long been recognized that further studies and elucidation of swirling flow dynamics and interactions with the flame (including PVC) could greatly benefit from velocity field measurements simultaneously with capturing distributions of the gas temperature, local fuel concentration, and shape of the flame front. Such a combined application of the PIV method and the planar laser-induced fluorescence (PLIF) for chemical species have already been performed in a number of papers to investigate the unsteady combustion and interaction of the coherent flow structures with flame.

Stöhr et al. (2011) [43] combined PIV with the PLIF of the hydroxyl radical (OH PLIF) to study methane combustion in a combustion chamber with flow swirl ($Re = 9000$ for non-reacting conditions). A pair of helical vortex structures was detected from the POD of the velocity fields. Based on the phase-averaged fluorescence intensity it was concluded that the coherent flow structures strongly influenced the flame shape. The authors concluded that a large-scale helical vortex in the inner mixing layer promoted combustion by intensifying the heat and mass exchange between the fresh mixture and the combustion products and by enlarging

the flame front surface. Time-resolved PIV and OH PLIF measurements for the same combustor geometry were performed by Boxx et al. [44] and later by Stöhr et al. [45] and others. Boxx et al. [46] observed the events of local flame extinction in regions with intensive flow strain, which did not lead to a blow-off of the entire flame. Additionally, isolated flame regions, probably caused by auto-ignition events, could be clearly seen in the OH PLIF images at the centres of the large-scale vortex structures.

In addition to the pair of helical vortices, Stöhr et al. [45] observed a central vortex spreading along the axis towards the exhaust tube of the combustion chamber. Based on a 3D reconstruction of the phase-averaged OH PLIF data, it was inferred that the flame zone was aligned with the inner helical vortex structure, which promoted combustion via enhanced mass exchange between the combustion products and fresh gas. Boxx et al. [46] compared the flow and flame dynamics for premixed methane/air flames in a swirl combustion chamber for cases with and without strong thermoacoustic oscillations. The flow/flame interaction has been analysed via time-resolved PIV and OH PLIF measurements. A bubble shaped recirculation zone and PVC were found for the flow when undergoing strong thermoacoustic pulsations, whereas the other case featured a conical shape of the recirculation zone without clear evidence of PVC. Additionally, in the former case, a strong coupling was detected between the unsteady flame and the PVC dynamics. Whereas coupling between large-scale vortex structures and flame front dynamics in swirl combustors have been demonstrated in a number of experiments, a better understanding of vortex structures' impact on unsteady heat release and thermoacoustic pulsations requires simultaneous measurements of the velocity fields and spatially resolved distributions of temperature/density or heat release. Such data have been provided by numerical simulations of some simple flames, (e.g., Duwig and Fuchs [40], Huang et al. [47]), but are still difficult to measure, especially in more complex flame configurations. Usually, line-of-sight chemiluminescence images are used for the analysis of the phase-averaged variations of heat release [48,49]. Giezendanner-Thoben et al. [50] used a combination of two OH PLIF systems (two-line PLIF) to measure the planar temperature fields in hot combustion products in a swirl combustion chamber. The 2D temperature distributions were phase-averaged according to the amplitude of the thermo-acoustic pulsations. The unsteady mode corresponded to nearly

symmetric variations (likewise in [48,49]) in the temperature in the inner recirculation zone. Thus, the contribution of the asymmetric mode (i.e., PVC with secondary vortices) to unsteady heat release is still unclear and requires further research [51].

A combined application of the HCHO PLIF and OH PLIF can be used to reveal zones of intensive heat release in lean hydrocarbon flames (e.g., [52,53]). The intersection of the OH and HCHO fluorescence regions serves as an indicator of the chemical reaction $\text{OH} + \text{CH}_2\text{O} \rightarrow \text{HCO} + \text{H}_2\text{O}$, which is an important step in the oxidation pathway of conventional hydrocarbons. The production rate of the highly reactive formyl radical (HCO) during this reaction limits the further production of CO and heat release. Mulla et al. [54] compared the feasibility of heat release rate measurements via HCHO and OH PLIF and by HCHO and H-atom PLIF for laminar premixed Bunsen flames. Both methods have provided close estimates for the heat-release rates, although the latter appears to be more complicated due to the two-photon excitation of the H fluorescence. Röder et al. [55] discussed the correlation between the visualization of regions with intensive local heat release rate based on OH* chemiluminescence (integrated along the line of sight) and the HCHO and OH PLIF in premixed methane/air swirling flames. The latter technique appears to be more accurate since it resolves spatial structures in a turbulent flame. The present paper reports on the impact of the coherent flow structures in a high-swirl turbulent jet with a vortex breakdown on large-scale deformations of the reaction zone in fuel-lean and fuel-rich flames. Three types of flames are considered as examples of typical combustion regimes for swirl burners, viz., V-type flames of fuel-lean and fuel-rich mixtures with the flame onset in the inner recirculation zone, and a partially premixed fuel-rich M-type lifted flame. The focus is placed on identifying the coupling between the regions of elevated local heat release rate and the location of the helical vortex structures in the flows. To reveal these regions in the fuel-lean flame, the HCHO and OH PLIF data were conditionally sampled (phase-averaged) according to the temporal coefficients of the velocity POD modes. For the fuel-rich lifted flame, the velocity divergence served as an indirect indicator of the intensive local heat release.

2 Experimental setup

The experiments reported here were conducted in unconfined swirling flames issuing from a burner that was used in our previous studies of flow with [30, 56] and without [35] combustion. The burner was designed as an axisymmetric contraction nozzle with a vane swirler mounted inside. The outlet nozzle diameter d was 15 mm. The geometry of the burner is shown in the inset of Figure 1. The diameter of the centre body supporting the vanes and the swirler are $d_1 = 7$ mm and $d_2 = 27$ mm, respectively. The inclination angle of the vanes relative to the axis is $\psi = 55^\circ$.

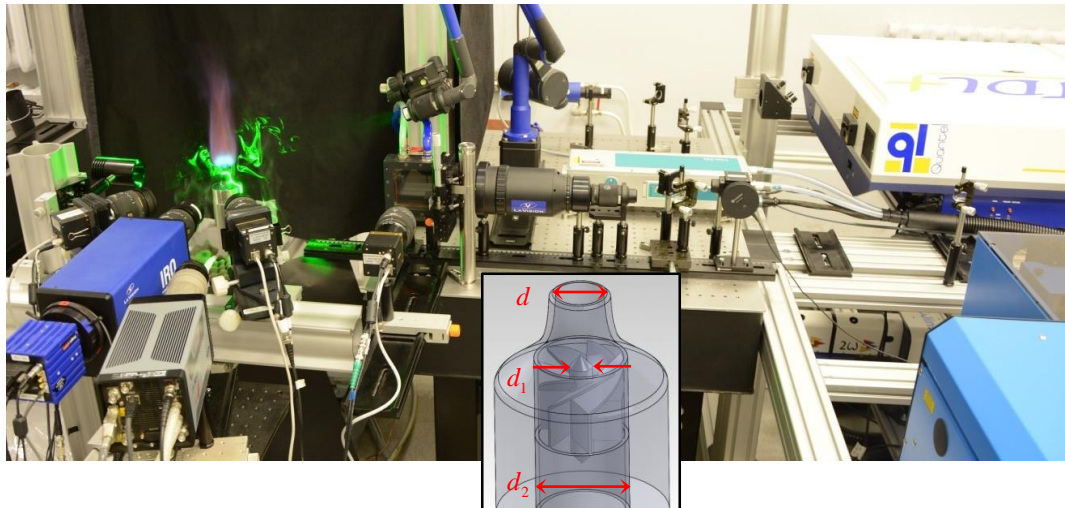
$$S = \frac{2}{3} \left(\frac{1 - (d_1/d_2)^3}{1 - (d_1/d_2)^2} \right) \tan(\psi)$$

The flow swirl rate S , defined on the basis of the swirler geometry [1], is equal to 1.0, which is well above the critical value of approximately 0.6 for vortex breakdown in flow without combustion. The distributions of the mean velocity components and the variances of the turbulent fluctuations at the vicinity of the nozzle exit are shown in Appendix A. An evaluation of the swirl rate from these data is also provided. The burner was connected to a mixing pipe that ensured complete mixing of the fuel (methane, 99.99%) and air inside the nozzle. The flowrates of the gases were controlled by mass flow meters (Bronkhorst El-Flow). The air was supplied by a pressure line, and upstream of the mixing pipe, it was passed through a seeder with TiO_2 particles with an average size of 0.5 μm . The seeder consists of a tank with a mechanical mixer at its bottom.

The measurements were performed by simultaneously using the stereoscopic PIV, OH PLIF and HCHO PLIF methods. A photograph of the setup is shown in Figure 1. The PIV system consisted of a few CCD cameras (ImperX IGV-B2020, 8 bit images with 2048×2048 pixels) equipped with optical lenses (Sigma AF 50 mm, $f\# = 2.8$, EX DG Macro), bandpass filters (Edmund Optics with 85% transmittance at 532 nm with a FWHM of 10 nm), a double-head pulsed laser (Beamtech Vlite-200, with 200 mJ per 7 ns pulse at 532 nm) and a synchronizing TTL generator. The PIV images were processed by an advanced cross-correlation algorithm with a continuous image shift and deformation (see Scarano [57] for definition). The final size of the interrogation windows was 32×32 pixels, and the spatial overlap rate was 50%. The PIV cameras were calibrated by using a multi-

level calibration target. The projection transformations of each camera were approximated by 3rd-order polynomial mapping functions [58]. After stereoscopic reconstruction, the spatial resolution of the three-component velocity field was 0.57 mm, and the grid spacing was 0.285 mm.

The OH PLIF system consisted of a tunable dye laser (Sirah Precision scan), a pulsed Nd:YAG pump laser (QuantaRay with approximately 1 J of energy per pulse at 532 nm), and a UV-sensitive intensified CCD camera (Princeton instruments PI-MAX-4, 16 bit images with 1024×1024 pixels). The camera was equipped with a UV-lens (LaVision 100 mm, $f\# = 2.8$) and a bandpass optical filter (LaVision with 20% transmittance at 307 nm with FWHM of 10 nm). To ensure that the $Q_1(8)$ line of the (1–0) band in the $A^2\Sigma^+ - X^2\Pi$ system was excited during the PLIF measurements, the excitation spectrum for the laminar premixed Bunsen flame was calibrated with reference to simulations using LifBase software [59]. The average pulse energy of the tunable laser was approximately 5 mJ for wavelengths in the range of 282–284 nm. The HCHO PLIF system was composed of a UV-sensitive image intensifier (LaVision IRO) and sCMOS camera (LaVision Imager sCMOS, 16 bit images with 2560×2160 pixels), equipped with an optical lens (Sigma AF 50 mm) and a set of optical filters (Edmund Optics Multi-Notch filter for Nd:YAG lasers, LaVision bandpass filter with 90% transmittance in the range 415–455 nm and a low-pass filter for 355 nm), and a pulsed Nd:YAG laser (QuantaRay Brilliant B with 90 mJ energy per pulse at 355 nm). The laser excited HCHO fluorescence during the 4_0^1 transition of the A–X band [60]. The exposure time of the PLIF images was 200 ns.



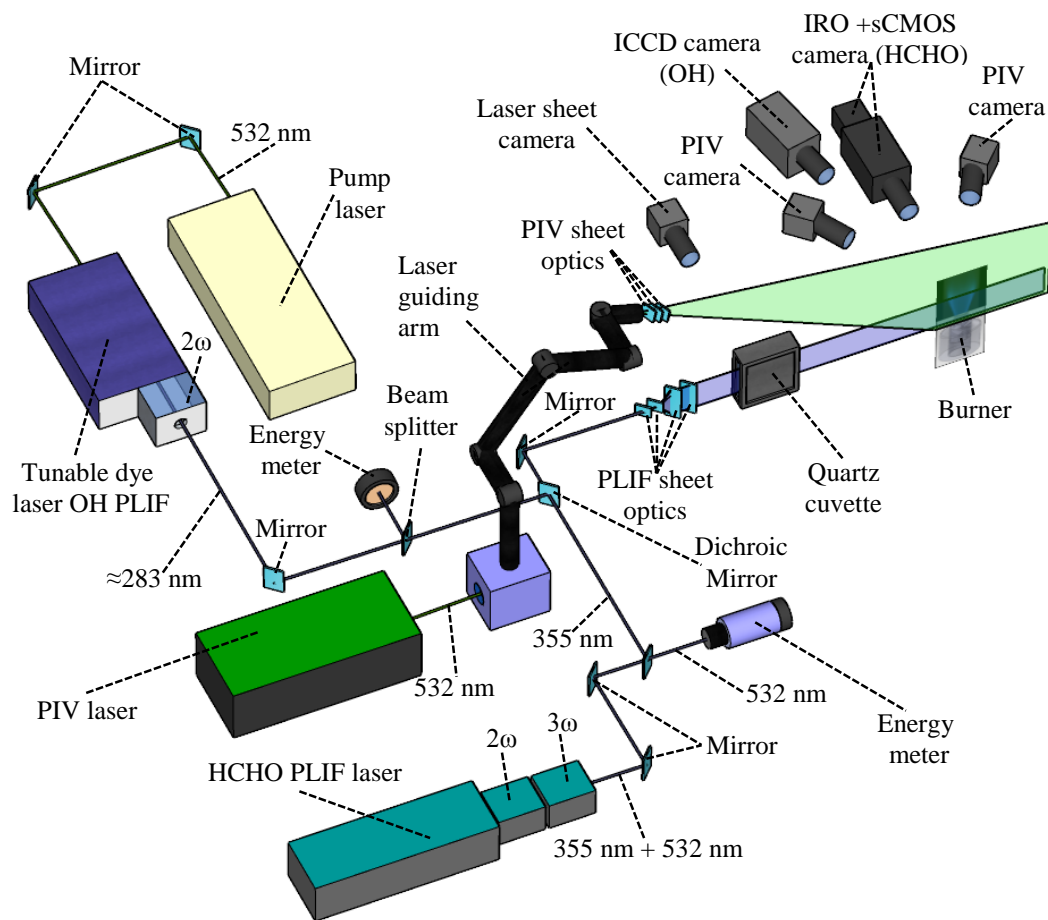


Fig. 1 Photograph and scheme of the experimental setup.

The beams of the PLIF systems were combined by using dichroic mirrors and converted to a collimated laser sheet with an approximate width of 50 mm and thickness of 0.8 mm in the region of interest. To ensure that the focus of both laser beams is located in the region of interest, the laser of the HCHO PLIF system could be shifted along the beam direction to ensure a similar length of the optical pass for the beams prior to the collimator. Two PLIF pulses, separated by 10 μ s, were shot between a pair of the PIV laser pulses. The PIV laser beam was converted into a diverging laser sheet (with a 0.8 mm thickness in the region of interest) by an optical guiding arm and a system of cylindrical and spherical lenses. A laser alignment paper was used to ensure that the laser sheets coincide well. The PLIF cameras were then calibrated in the same way as the PIV cameras. After correcting the perspective on the PLIF images, they were processed by a set of mathematical algorithms, including correction of the spatial non-uniformity of the laser-sheets and sensitivity of the sensors, removal of the background, dark-current and reflections. Additionally, a Canny edge filter was used to remove isolated bright dots in the

HCHO PLIF images (cf., Figures 3 and B1). The non-uniform sensitivity was tested by imaging a white paper that was placed out of focus. To account for the non-uniformity of both PLIF laser sheets, an additional CCD camera (ImperX IGV-B2020) monitored the fluorescence intensity inside a cuvette filled with a solution of Rhodamine 6G. The cuvette was placed after the collimator.

The obtained PLIF intensity was spatially sampled to the same spatial grid as the PIV data with the same resolution. The effect of spatial averaging on the PLIF data is shown in Appendix B. To reveal coherent structures, the PIV data (region x/d from -1.2 to 1.2 , y/d from 0 to 2.5) was processed by a snapshot POD method [32], based on a singular value decomposition [61]. For each flow/flame case the set of fluctuating velocity fields $\mathbf{W} = [\mathbf{u}'(\mathbf{x}, t_1) \dots \mathbf{u}'(\mathbf{x}, t_N)]$ was decomposed into a series of orthonormal POD modes $\mathbf{U} = [\boldsymbol{\phi}_1(\mathbf{x}) \dots \boldsymbol{\phi}_M(\mathbf{x})]$, multiplied by the normalized temporal coefficients $\alpha_q(t)$:

$$\mathbf{W} = \mathbf{U}\boldsymbol{\Sigma}\mathbf{V}^T \quad \text{or} \quad \mathbf{u}'(\mathbf{x}, t_k) = \sum_{q=1}^N \alpha_q(t_k) \sigma_q \boldsymbol{\phi}_q(\mathbf{x}),$$

$$\text{where } \mathbf{U}\mathbf{U}^T = \mathbf{I}_M \quad \text{and} \quad \mathbf{V}\mathbf{V}^T = \mathbf{I}_N,$$

$$\sum_{k=1}^M \boldsymbol{\phi}_i(\mathbf{x}_k) \boldsymbol{\phi}_j(\mathbf{x}_k) = \delta_{ij} \quad \text{and} \quad \sum_{k=1}^N \alpha_i(t_k) \alpha_j(t_k) = \delta_{ij}.$$

The singular values σ_q ($\boldsymbol{\Sigma} = \text{diag}[\sigma_1 \dots \sigma_N]$) are positive and listed in descending order. They characterize the amplitude of the modes and correspond to the square root of the POD eigenfunctions λ , which is used in other common notation. \mathbf{I} is the identity matrix. M and N correspond to the number of spatial points and temporal samples (snapshots), respectively.

Low-dimensional modelling of turbulent flow dynamics relies on the use of a limited number of POD modes. Additionally, when the considered flow is characterized by intensive quasiperiodic velocity fluctuations, two first POD modes could be used to obtain the phase-averaged velocity pattern [30,43, 62], where ϕ is the phase of the quasiperiodic process.

$$\mathbf{u}'_c(\mathbf{x}, \phi) = \left(\sigma_1/\sqrt{N}\right) \sin(\phi) \boldsymbol{\phi}_1(\mathbf{x}) + \left(\sigma_2/\sqrt{N}\right) \cos(\phi) \boldsymbol{\phi}_2(\mathbf{x}).$$

Thus, two POD modes correspond to the phase-shifted coherent velocity fluctuations:

$$\left(\sigma_1/\sqrt{N}\right)\boldsymbol{\phi}_1 = \mathbf{u}_c''(\phi = \pi/2) = \mathbf{u}_1'' \text{ and } \left(\sigma_2/\sqrt{N}\right)\boldsymbol{\phi}_2 = \mathbf{u}_c''(\phi = 0) = \mathbf{u}_2''.$$

The effect of possible phase jitter is discussed in Legrand et al. [63] and Stohr et al. [43], where the low-dimensional model based on the first two POD modes is compared with the phase-averaged velocity fields.

In other words, the POD provides the coherent part \mathbf{u}_c'' of the velocity fluctuations in the framework of the triple decomposition of Hussain and Reynolds [64] via conditional sampling of the instantaneous fields (see also Antonia [65]). In general, each POD mode can be expressed as the linear combination of the instantaneous velocity fields:

$$\mathbf{U} = \mathbf{W}\boldsymbol{\Sigma}^{-1}\mathbf{V} \text{ or } \boldsymbol{\phi}_q(\mathbf{x}) = \sum_{k=1}^N a_{qk} \mathbf{u}'(\mathbf{x}, t_k) \sigma_q^{-1}.$$

Therefore, the passive scalar fluctuations $\mathbf{C} = [c'(\mathbf{x}, t_1) \dots c'(\mathbf{x}, t_N)]$ can also be conditionally sampled $\mathbf{C}\boldsymbol{\Sigma}^{-1}\mathbf{V}$ based on the temporal coefficients of the velocity POD modes \mathbf{V} (similar to Duwig and Fuchs [40]). Thus, taking σ_q into account, the low-dimensional model of the coherent passive scalar fluctuations can be written as:

$$c_q''(\mathbf{x}) = \left(1/\sqrt{N}\right) \sum_{k=1}^N a_{qk} c'(\mathbf{x}, t_k)$$

Results

Figure 2 shows photographs of the four flames considered here, displaying qualitatively their main features: a laminar Bunsen flame ($\text{Re}_{air} = 1\,500$, $\Phi = 0.9$), turbulent swirling flames ($\text{Re}_{air} = 5000$) of lean and rich mixtures ($\Phi = 0.7$ and 1.4 , respectively) and a partially premixed lifted flame ($\Phi = 2.5$). Specifications of the cases considered are summarized in Table 1.

Table 1: Cases considered: swirl rate $S = 1.0$, defined as in [1], Bunsen flame $S = 0$.

Flow/ flame	Bunsen flame (no swirl)	Non- reacting swirling jet	Fuel-rich lifted flame	Fuel-rich premixed flame	Fuel-lean premixed flame
Re_{air}	1500	5000	5000	5000	5000
Equivalence ratio Φ	0.9	0.0	2.5	1.4	0.7

The flame shapes are similar to those of the earlier studied flames of propane/air mixtures for the same swirl burner geometry, [56]. The premixed swirling flames have a cone-like shape and penetrate into the nozzle. The lifted swirling flame is more turbulent and stabilized at a certain height above the nozzle exit.

To illustrate the visualization potential of the PLIF techniques when using different fluorescent agents, Figure 3 shows an instantaneous snapshot of the PLIF and PIV data for a generic Bunsen flame using OH, HCHO and their combination. The OH PLIF in Figure 3(a) visualizes both the flame front and the combustion products. The HCHO fluorescence identifies the preheat zone of the flame front, whereas the intersection of the OH and HCHO fluorescence visualizes the zone of the most intensive heat release rate, which coincides with the visible flame front in Figure 2.

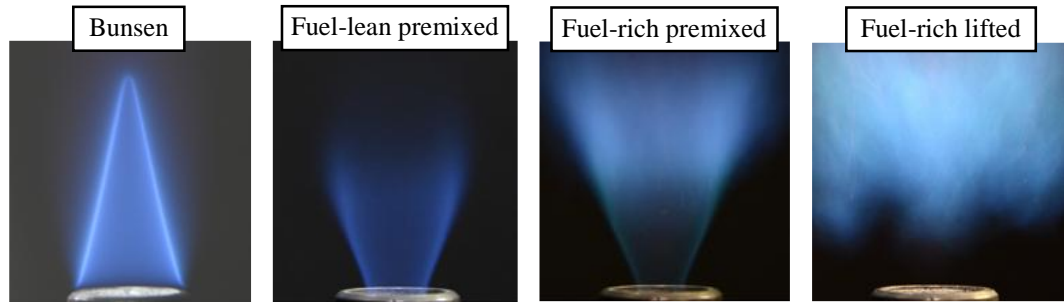


Fig. 2 Images of the studied flames.

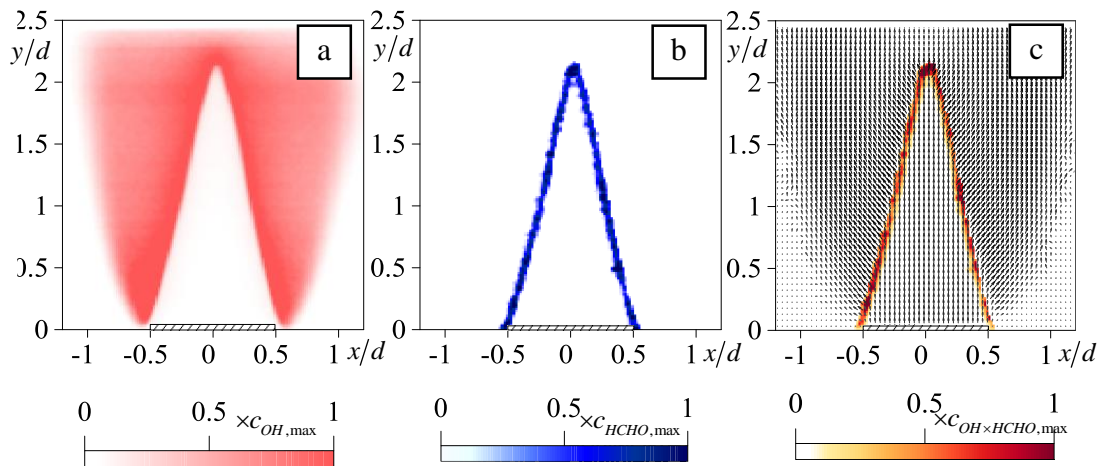


Fig. 3 Instantaneous snapshot of the PIV and PLIF data for the Bunsen flame. (a) OH PLIF, (b) HCHO PLIF, (c) PIV and OH×HCHO PLIF. $c_{HCHO,max} = 1830$, $c_{OH,max} = 31800$.

Figure 4(a) shows a 3D reconstruction of the flame shape based on the OH×HCHO PLIF data and an assumption of the axial symmetry. Figure 4(b) demonstrates that the positive divergence (dilatation rate [66]) of the velocity field serves as an

indirect indicator of the flame front location (region with an intensive heat release). This follows from the continuity of the medium and a negative density gradient along the streamlines, where they intersect the flame front.

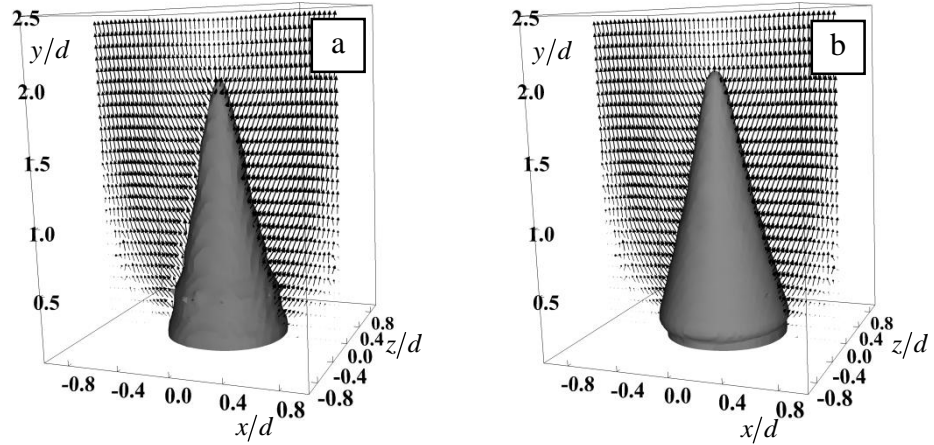


Fig. 4 3D visualization of the flame front for the Bunsen flame. (a) $\text{OH} \times \text{HCHO}$ PLIF signal, (b) positive divergence of the velocity field ($\text{div}\mathbf{U} = 4U_0/d$).

Non-reacting swirling jet flow

To identify the effects of helical vortex structures on different flames and the mutual interaction of the combustion and vortex dynamics, for reference we first provide some results from the velocity and vorticity fields in a non-reacting swirling jet with the same configuration, swirl and Reynolds number, $\text{Re}_{\text{air}} = 5000$. The time-averaged and instantaneous velocity fields in the non-reacting jet are shown in Figure 5. The vectors correspond to 2D projections of the velocity vectors in the $x - y$ plane, with a colour visualization of the normal-to-plane (z direction) velocity component. For the time-averaged field, in Figure 5(a) the solid line is the contour of $U_y = 0$, thus visualizing a bubble-type central recirculation zone where $U_y < 0$. The profiles of the y and z components of the mean velocity at three selected heights are shown in Figure 6.

According to the axial velocity profile, there are two typical mixing layers in the flow, viz., the inner mixing layer between the annular jet and recirculation zone and the outer mixing layer between the jet and the surrounding air. Figures 5(c) shows the distribution of the turbulent kinetic energy, indicating the intensive velocity fluctuations over the entire field, and especially in the outer U-shaped jet region. Its maximum, located at the jet origin just above the centre of the nozzle exit, exceeds

the bulk velocity U_0 by 65%. As Figure 5(c) indicates, the instantaneous velocity pattern is sufficiently different from the mean flow due to the intensive fluctuations. The solid lines correspond to the contours of the positive values of a 2D modification of the vortex education Q-criterion [67] for the x-y plane

$$Q^{2D} = -\frac{1}{2} \frac{\partial u_x}{\partial x} \frac{\partial u_x}{\partial x} - \frac{1}{2} \frac{\partial u_y}{\partial y} \frac{\partial u_y}{\partial y} - \frac{\partial u_x}{\partial y} \frac{\partial u_y}{\partial x},$$

and visualize the cores of large-scale vortex structures that intersect the measurement plane. The vortices roll-up both in the inner and outer mixing layers.

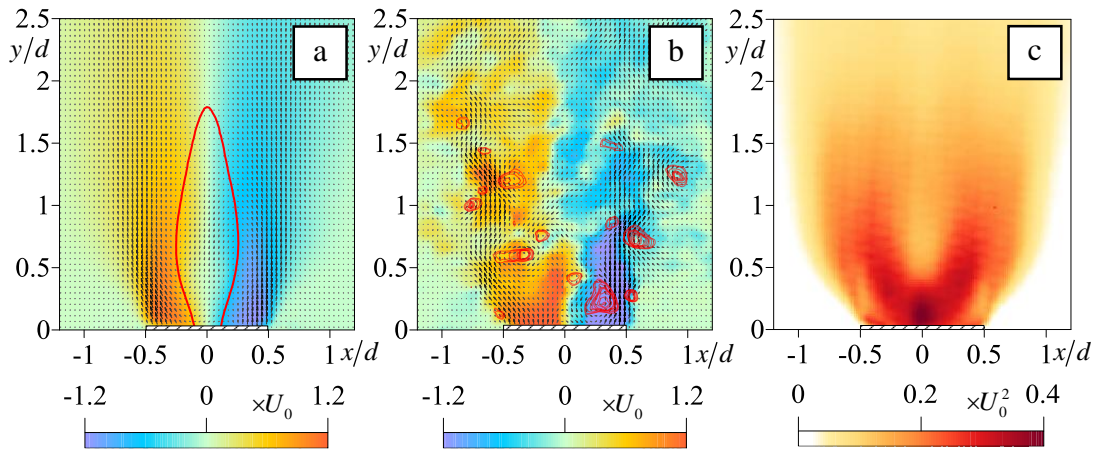


Fig. 5 Distributions of the (a) time-averaged (solid line shows a contour of $U_y=0$) and (b) instantaneous (solid lines show contours of $Q^{2D} = 4(2+n)U_0^2 d^{-2}$, where n is a positive integer) velocity fields and (c) the turbulent kinetic energy in the non-reacting swirling jet.

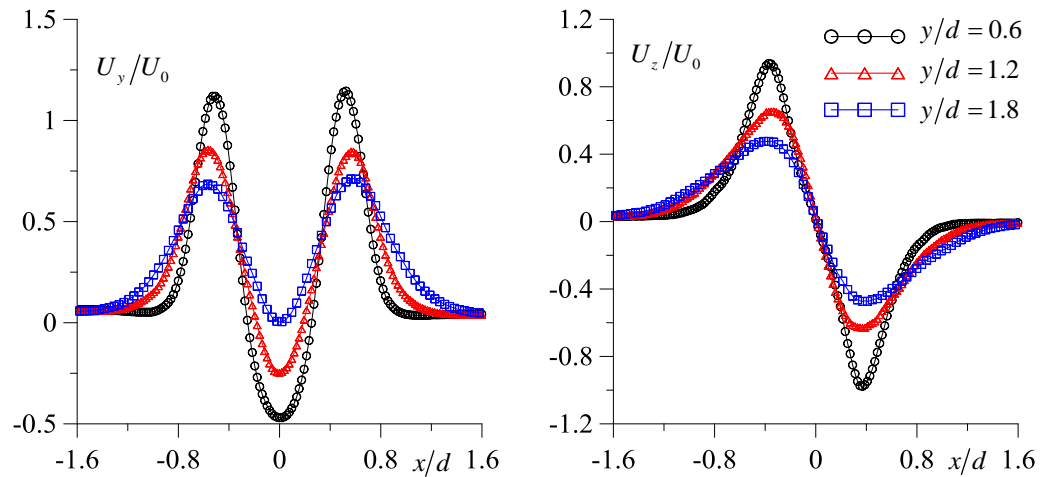


Fig. 6 Profiles of the axial and azimuthal velocity components for the non-reacting swirling jet.

To reveal coherent velocity fluctuations, the PIV data are processed by the POD. The POD spectrum (compared with those for the reacting flows) is shown in Figure 7. The first two POD modes for the non-reacting flow include more than 15% of

the spatially averaged turbulent kinetic energy, whereas the energy of every other mode is below 2%. According to the scatter of the temporal coefficients of the first two POD modes around the circle-like Lissajous figure shown in Figure 7(b), these modes are statistically correlated.

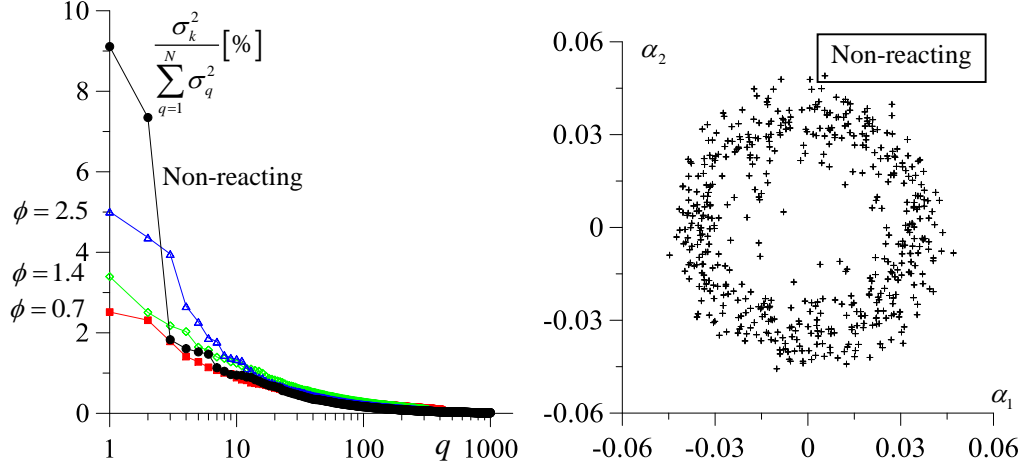


Fig. 7 (a) POD spectra for the non-reacting and reacting swirling jets, (b) Temporal coefficients for the first two POD modes for the non-reacting case.

Figure 8 shows the spatial distributions of the first four POD modes. The z -component of the velocity fluctuations is visualized using colours. The spatial distributions of the coherent velocity fluctuations in modes one and two are similar to those in previous studies, including 3D measurements by Alekseenko et al. [33], where it was shown that these two POD modes correspond to two orthogonal cross-sections of a single rotating coherent structure. A 3D shape of the coherent structure can be reconstructed by assuming that the increment of the azimuthal angle θ is equal to that of the phase angle ϕ of the 2D phase-averaged velocity pattern, obtained from the first two POD modes. The rotation direction of the coherent structure relatively to the jet swirl is based on the vortices winding direction from the previous 3D study [33].

Figure 9(a) shows the phase-averaged values of the velocity of the flow $\mathbf{U} + \mathbf{u}_1''$ (i.e., $\phi = \pi/2$) and concentration $C + c_1''$ of a passive scalar added to the jet (acetone vapor). The 2D Q-criterion is plotted to visualize the large-scale vortex structures present in both the inner and outer mixing layers. These structures are located in an asymmetric manner and are found to be cross-sections of a pair of spiralling vortices [33]. Figure 9(b) provides visualization of the 3D reconstruction $\mathbf{U} + \mathbf{u}_c''$, where large-scale vortex structures are visualized by using the full 3D formulation of the

Q-criterion. The coherent structure corresponds to the vortex core spiralling around the central recirculation zone. The primary vortex structure is surrounded by a secondary helical vortex that is located in the outer mixing layer. Figure 9(b) also visualizes the sign of the coherent concentration fluctuations c_c'' to demonstrate that the outer helix transports the admixture out of the jet and induces positive coherent fluctuations in the outer mixing layer.

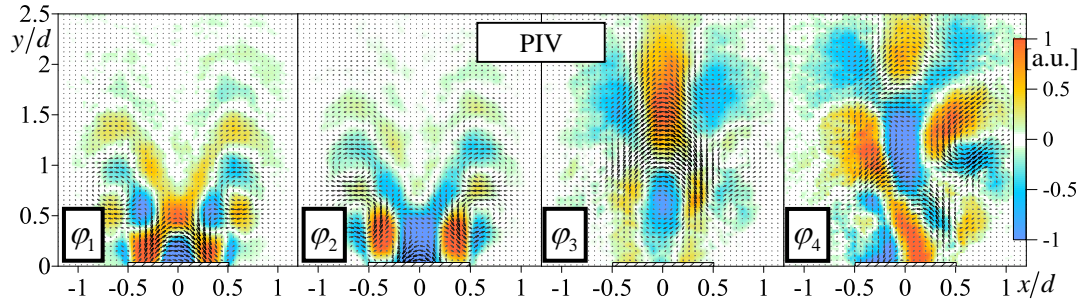


Fig. 8 Spatial distributions of the first four POD modes for the non-reacting swirling jet.

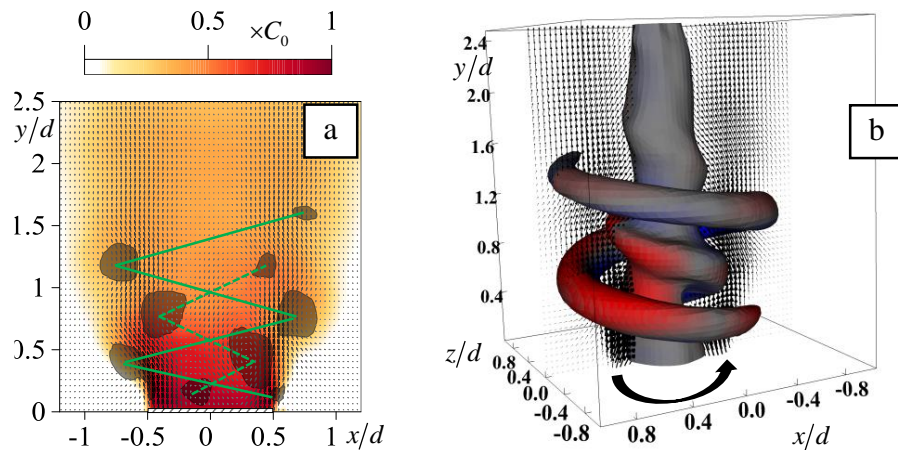


Fig. 9 Phase-averaged velocity and large-scale vortex structures in the non-reacting swirling jet. (a) Passive scalar phase-averaged concentration, (b) Regions of negative and positive coherent fluctuations of the concentration ($\blacksquare c_c'' < 0$, $\blacksquare c_c'' > 0$). The grey regions correspond to (a) $Q^{2D} > 1.2U_0^2d^2$ and (b) $Q^{3D} > 1.2U_0^2d^2$.

Fuel-rich lifted swirling flame

The instantaneous PIV and PLIF data for the fuel-rich lifted flame are shown in Figure 10. The flow is featured by a vortex breakdown with an unsteady central recirculation zone and a number of large-scale vortex structures, which are present in both mixing layers. According to the OH and HCHO fluorescence, the

combustion takes place in both the inner and outer mixing layers. The combustion products are trapped by the central recirculation zone and transported upstream, where they mix with the fresh gas (fuel-rich methane/air mixture with $\Phi = 2.5$) issuing from the nozzle. The flame base is also stabilized in the low-velocity region of the outer mixing layer (marked by arrows), where the jet mixes with the surrounding air.

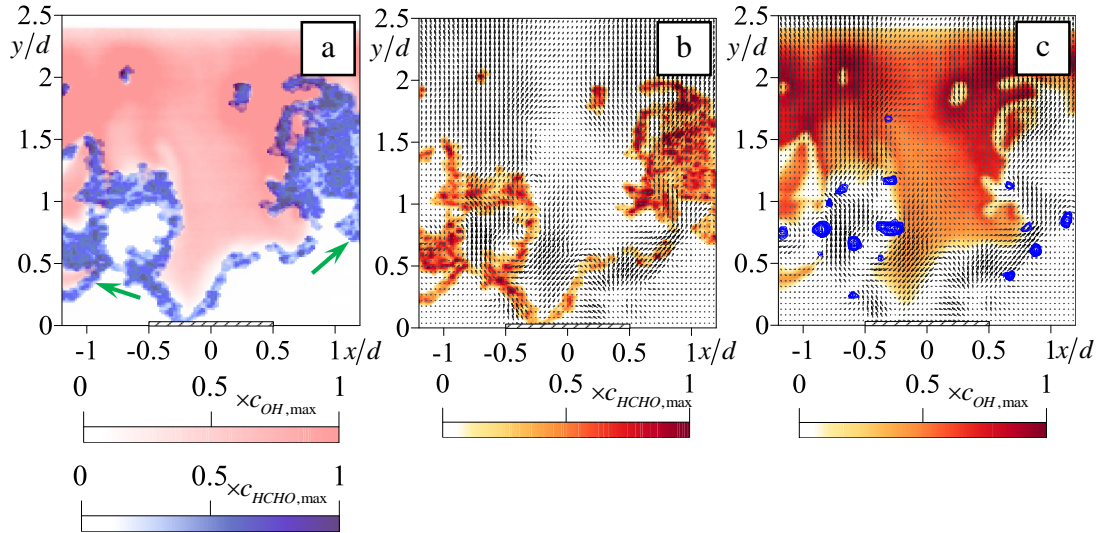


Fig. 10 Instantaneous snapshot of the PIV and PLIF data for the fuel-rich lifted flame ($\Phi = 2.5$). (a) OH PLIF and HCHO PLIF, (b) PIV and HCHO PLIF, (c) PIV and OH PLIF (solid lines correspond to $Q^{2D} > 3.1(2 + n)U_0^2 d^{-2}$). $c_{HCHO,max} = 1360$, $c_{OH,max} = 25600$.

The POD spectrum of the velocity fluctuations for this flow case is shown in Figure 7(a). There are POD modes with considerably greater amplitudes than that of the other modes. The first four POD modes are shown in Figure 11, where the conditionally sampled fluctuations c_1'' , c_2'' , c_3'' and c_4'' of the OH and HCHO fluorescence intensity are also shown. The velocity data is in agreement with a previous study by Alekseenko et al. [30]. The second and third mode correspond to coherent velocity fluctuations, which are similar to those observed in the non-reacting jet before ignition of the flame. The first POD mode corresponds to the unsteady entrainment of surrounding air and oscillations of the axial velocity of the combustion products induced by the buoyancy force. The conditionally sampled OH and HCHO PLIF data for this mode show nearly symmetric oscillations of the fluorescence intensity, whereas for the second and third modes the conditionally sampled PLIF data appear to be almost asymmetric.

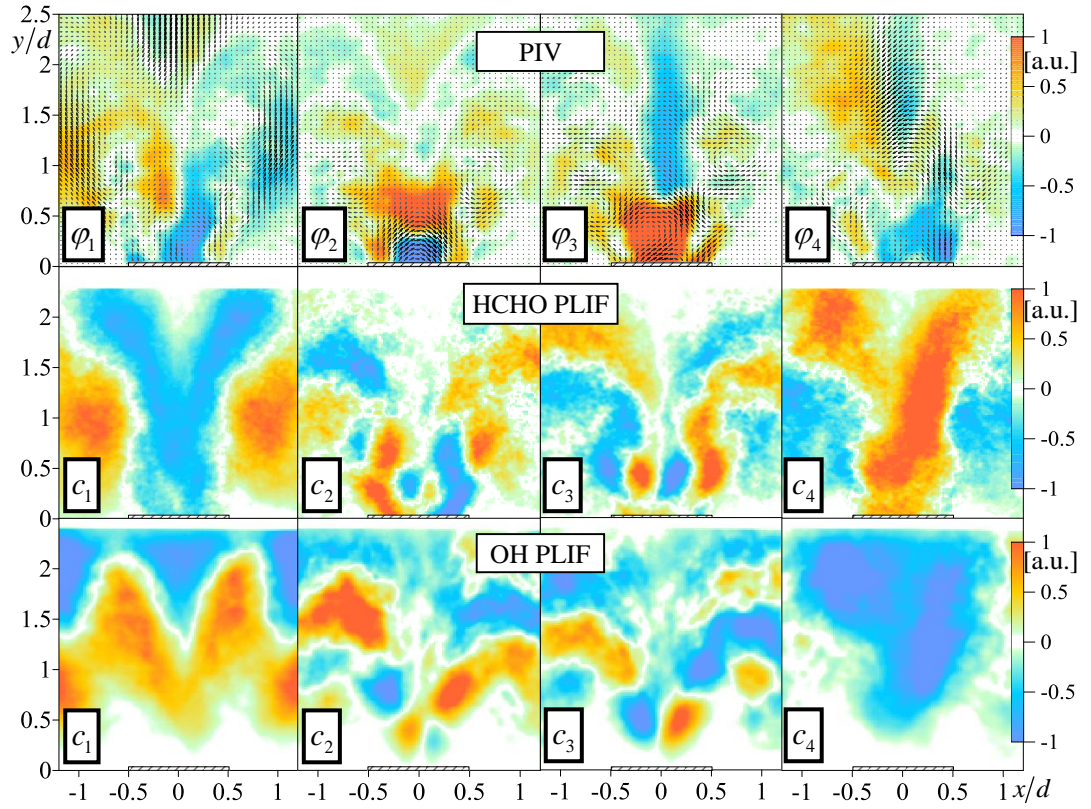


Fig. 11 Spatial distributions of the first four POD modes and the conditionally sampled PLIF data for the fuel-rich lifted flame ($\Phi = 2.5$).

Figure 12(a) depicts the phase-averaged velocity field $\mathbf{U} + \mathbf{u}_2''$ and OH PLIF intensity ($C + c_2''$, where C is the mean PLIF intensity and c_2'' is the conditionally sampled value of the intensity fluctuations according to the temporal coefficients of the second POD mode). The velocity data show that the coherent velocity fluctuations are induced by large-scale vortex structures in the inner and outer mixing layers, each forming a zig-zag pattern. The smoothed shape of the flame front reveals that the helical vortex structures produce large-scale deformations of the reaction zone (after the smaller-scale turbulent corrugations were filtered out during conditional sampling). The arrow shows that the phase-averaged location of the flame base in the outer layer is close to the outer large-scale vortex structure. Similar to the previous study [30], the second and third POD modes are used to obtain a 3D reconstruction of the coherent flow structure (including PVC) shown in Figure 12(b) and (c). The 3D reconstruction of the smoothed flame shape is obtained based on the coherent fluctuations c_2'' and c_3'' of the OH PLIF data. The coherent structure consists of the primary vortex core and a pair of secondary helical

vortices. The magnitude of the conditionally sampled divergence of the velocity field $\mathbf{U} + \mathbf{u}_c''$ (divergence and conditional sampling are linear operators and thus commute) indicates that the helical vortex in the outer mixing layer is correlated with a decrease in the local density during combustion and heat release. This is expected because the outer vortex structure locally intensifies mass exchange by engulfing the surrounding air into the jet and delivering the fuel into a low-velocity outer mixing layer where the flame base is located.

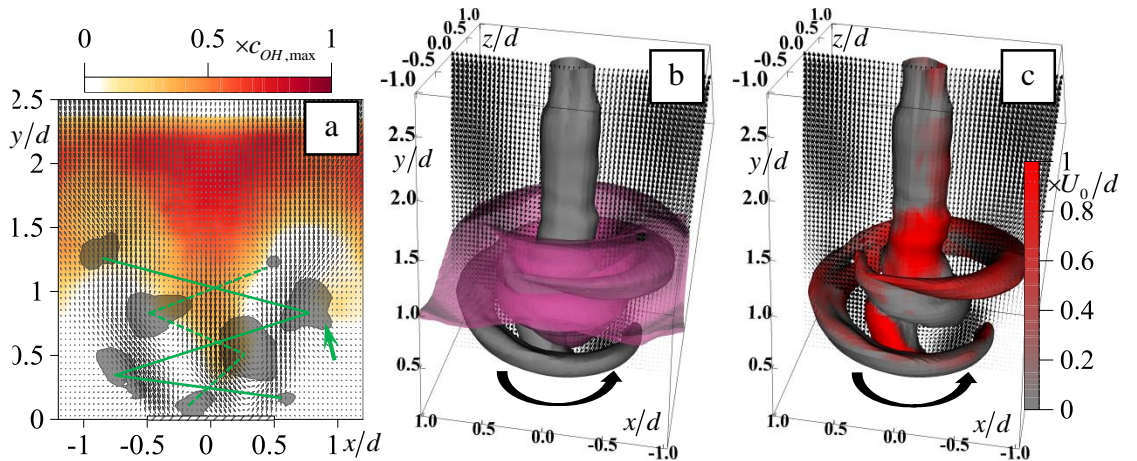


Fig. 12 Phase-averaged velocity and large-scale vortex structures in the fuel-rich lifted flame ($\Phi = 2.5$). (a, b) Phase-averaged OH PLIF, (c) Positive velocity divergence. The grey regions correspond to (a) $Q^{2D} > 1.22U_0^2d^{-2}$ and (b,c) $Q^{3D} > 1.22U_0^2d^{-2}$. $c_{OH,max} = 25600$.

Fuel-rich premixed swirling flame

The instantaneous snapshots of the PIV and PLIF data for the fuel-rich premixed flame are shown in Figure 13. The flame front has the shape of a corrugated cone that surrounds the central recirculation zone, containing hot combustion products. When the annular jet issues from the nozzle, the flame front is stabilized in the inner mixing layer. Downstream it shifts towards the outer mixing layer, where afterburning occurs during jet mixing with the surrounding air. According to the Q-criterion, large-scale vortex structures are present in both the inner and outer mixing layers.

The first four POD modes for this flow and the coherent fluctuations of the PLIF data are shown in Figure 14. The velocity modes are rather different from those detected in the non-reacting flow and fuel-rich lifted flame. They correspond to the velocity fluctuations mainly in the upper part of the recirculation zone, which

produce variations in the OH and HCHO fluorescence intensities. The distributions do not provide clear evidence that helical vortex structures have strong impact on the flow dynamics for this type of flame.

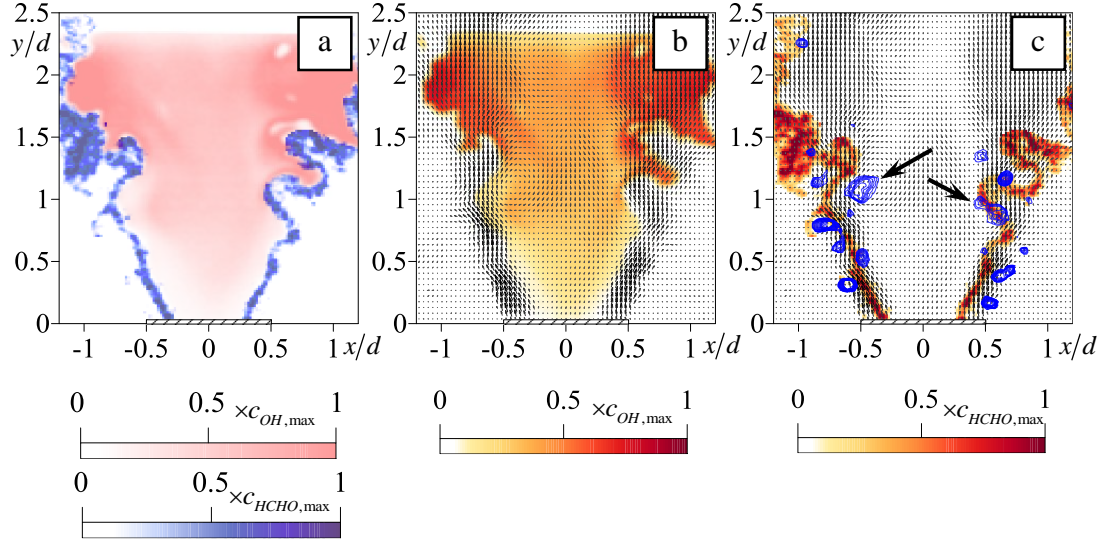


Fig. 13 Instantaneous snapshot of the PIV and PLIF data for the fuel-rich premixed flame ($\Phi = 1.4$). (a) OH PLIF and HCHO PLIF, (b) PIV and OH PLIF, (c) PIV and HCHO PLIF (solid lines correspond to $Q^{2D} > 4(2 + n)U_0^2 d^{-2}$). $c_{HCHO, \max} = 1360$, $c_{OH, \max} = 25600$.

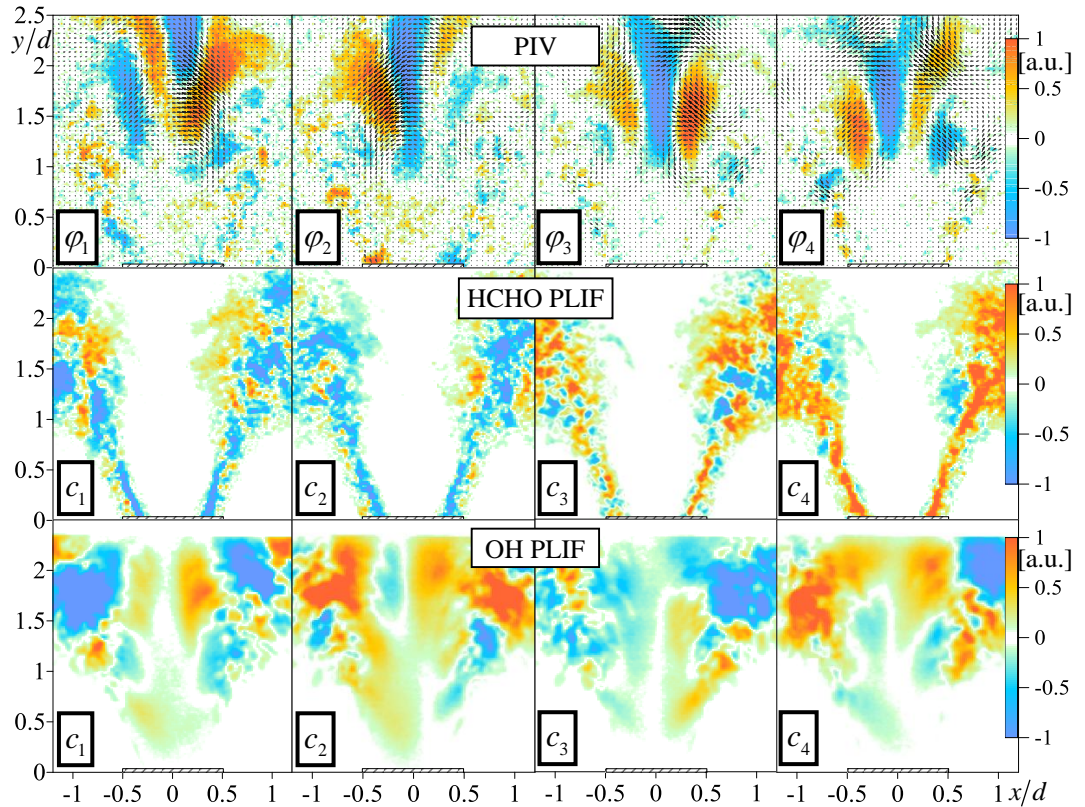


Fig. 14 Spatial distributions of the first four POD modes and conditionally sampled PLIF data for the fuel-rich premixed flame ($\Phi = 1.4$).

Fuel-lean swirling flame

The examples of the instantaneous PIV and PLIF data, which were captured simultaneously for the fuel-lean premixed flame, are shown in Figure 15. According to the HCHO signal in Figure 15(a), the flame front is situated in the inner mixing layer and envelopes the central recirculation zone, containing hot combustion products with intense OH fluorescence. The PLIF data also demonstrates a possible local extinction of the flame during wrinkling, indicated by the arrow in Figure 15(b). Large-scale vortex structures, forming a zig-zag pattern in the inner mixing layer, are clearly visible (marked by arrows in Figure 15(c)). In the present case, the intersection of the OH and HCHO signals provides information about regions with intensive heat release rates. The intensity of the OH×HCHO signal varies significantly along the flame front (Figure 15(c)) due to different local temperatures. The large-scale vortex structure in the inner mixing layer intensifies the heat and mass transfer between the combustion products and fresh mixture, locally enlarging the flame front and promoting combustion.

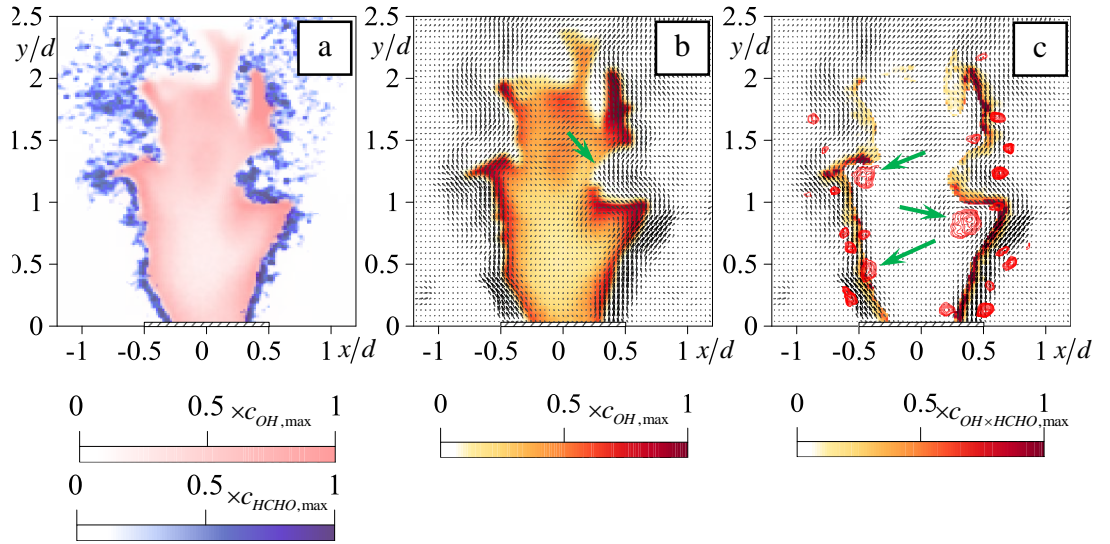


Fig. 15 Instantaneous snapshot of the PIV and PLIF data for the fuel-lean premixed flame ($\Phi = 0.7$). (a) OH PLIF and HCHO PLIF, (b) PIV and OH PLIF, (c) PIV and OH×HCHO PLIF (the solid lines correspond to $Q^{2D} > 4(2+n)U_0^2d^{-2}$). $c_{HCHO,max} = 1360$, $c_{OH,max} = 10200$.

To quantify the correlation between the propagation of the large-scale vortex structures and variation in the OH×HCHO fluorescence intensity, the velocity data

are processed by the POD, and the PLIF data fluctuations are conditionally sampled according to the temporal coefficients of the POD modes. Coherent fluctuations of the $\text{OH}\times\text{HCHO}$ fluorescence intensity are obtained directly by conditional sampling the values of the product, which are proportional to the local heat release rate. The first four POD modes are shown in Figure 16. Coherent velocity fluctuations in the first two POD modes appear to be similar to those for the non-reacting flow. The third and fourth POD modes correspond to the velocity fluctuations mainly in the upper part of the recirculation zone, which are similar to those detected for the fuel rich flame with $\Phi = 1.4$.

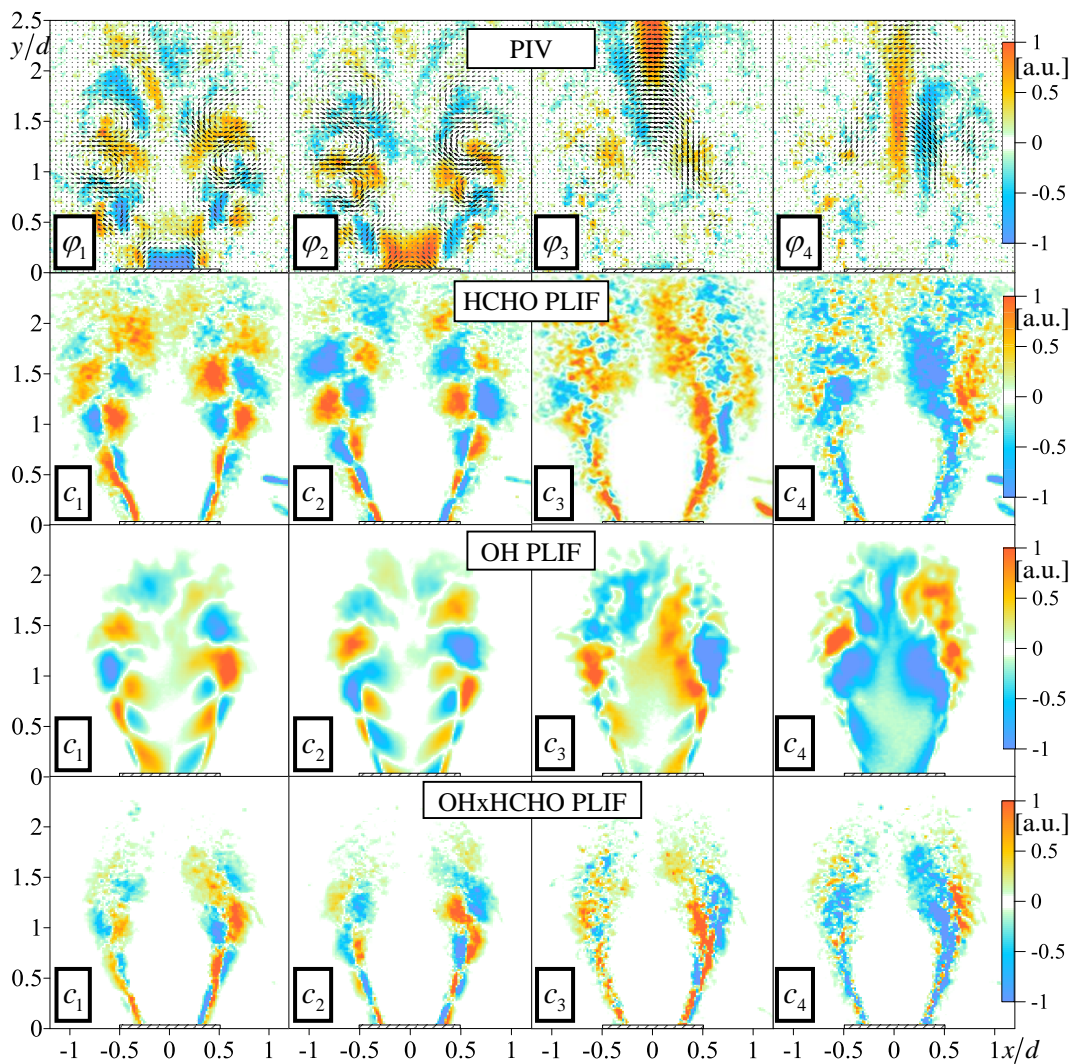


Fig. 16 Spatial distributions of the first four POD modes and conditionally sampled PLIF data for the fuel-lean premixed flame ($\Phi = 0.7$).

According to the coherent fluctuations of the HCHO PLIF intensity for the first and second POD modes, the coherent velocity fluctuations are correlated with regular flame front deformations, which correspond to travelling waves growing downstream. These flame front deformations take place simultaneously with a variation in the shape of the central recirculation zone (according to the coherent fluctuations of the OH PLIF data). Additionally, according to the conditionally sampled product of OH and HCHO fluorescence, these corrugations of the flame front are statistically correlated with variations in the OH×HCHO intensity, which are proportional to local heat release rate.

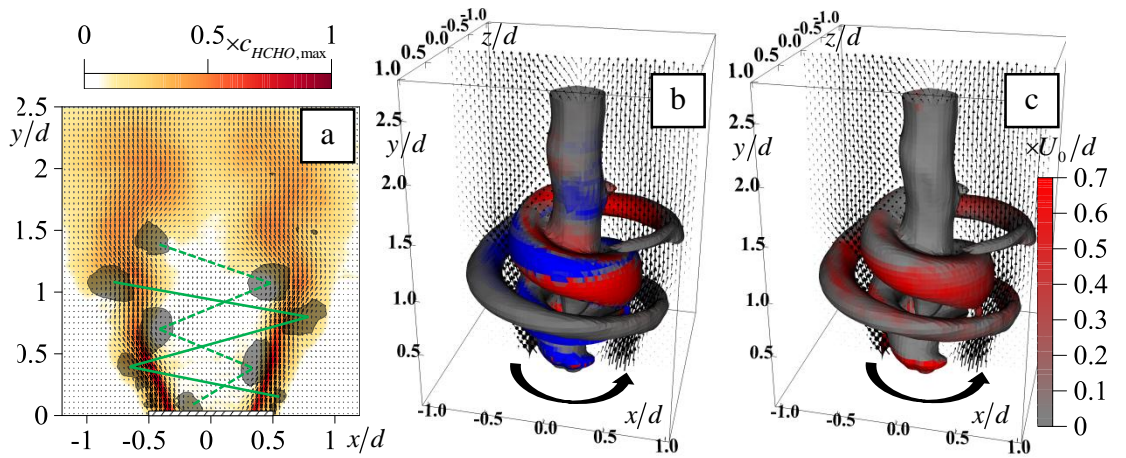


Fig. 17. The phase-averaged velocity and large-scale vortex structures in the fuel-lean flame ($\Phi = 0.7$). (a) The phase-averaged HCHO PLIF, (b) Regions of positive and negative coherent pulsations of the heat release rate ($\blacksquare c_c'' < 0$, $\blacksquare c_c'' > 0$), (c) Positive velocity divergence. The grey regions correspond to (a) $Q^{2D} > 2.25U_0^2d^{-2}$ and (b,c) $Q^{3D} > 2.25U_0^2d^{-2}$. $c_{HCHO, \max} = 1360$.

Figure 17(a) shows the phase-averaged velocity field ($\mathbf{U} + \mathbf{u}_1''$) and the shape of the flame front ($C + c_1''$ for the HCHO data) when the corrugations induced by non-coherent velocity fluctuations were smoothed during phase-averaging. The inner vortex structures, situated in a zig-zag pattern, are accompanied by a large-scale vortex structure in the outer mixing layer. A 3D reconstruction of the coherent flow structure based on the first and second POD modes ($\mathbf{U} + \mathbf{u}_c''$) shows that a pair of co-rotating helical vortex structures wind around the central vortex core, similar to that for the fuel-rich lifted flame. Figure 17(b) highlights regions with positive and negative values of coherent fluctuations of OH×HCHO fluorescence, corresponding to the minimal and maximal heat release rates. The inner helical

vortex is thus correlated with the maximal rates. Figure 17(c) highlights the region with positive values of the conditionally sampled dilatation rate (divergence of the velocity fields). According to the divergence, the gas density decreases during the chemical reaction between the inner and outer helical vortex structures and is correlated with the region of maximal heat release rates from OH×HCHO fluorescence.

Conclusions

The effects and impact of the coherent helical vortex structures on the shape and heat release in three unconfined swirling methane/air flames with vortex breakdown have been studied experimentally by simultaneously using a stereoscopic PIV with data processed by the POD, and the OH and HCHO PLIF techniques. Considered were fuel-lean and fuel-rich premixed flames and a partially premixed fuel-rich lifted flame, which all had the same burner configuration and the same Reynolds ($Re = 5000$) and swirl numbers ($S = 1.0$). For reference, the velocity field and helical vortex structures in a non-reacting swirling jet at the same conditions were analysed by the PIV, whereas the PLIF methods were applied to visualize the flame features in a non-swirling Bunsen laminar flame. Based on the measurements of the PIV velocity fields and the OH PLIF and HCHO PLIF flame visualization, qualitative correlations were established between the shape of the large-scale helical structures and large-scale deformations of the reaction zone for methane/air flames with different equivalence ratios. The following conclusions emerged from the study:

- As previously reported [33], the non-reacting swirling jet at the considered high swirl with a pronounced vortex breakdown and a central recirculating zone revealed double coaxial helix structures that winded in the direction opposite of the jet swirl and were located in the two coaxial mixing layers, namely, the inner one enveloping the recirculation bubble and the external one between the jet and the surrounding air.
- What matters more are the effects of the coherent helical structures on the combustion compared to non-swirling flames at the same conditions, and especially their impacts on the flame shape and the heat release.

- The POD of the velocity fields measured by the PIV revealed that, just as in the non-reacting jet, coherent flow structures were also detected in the reacting jet flows, consisting of large-scale helical vortices, including the PVC, with the primary vortex core accompanied by two secondary helical vortex structures.
- Based on the conditional sampling of the OH PLIF and HCHO PLIF fluctuations, as well as their product, it is found that the positions of the secondary helical structures are coupled with large-scale deformations of the reaction zone of the fuel-lean premixed flame and of the partially premixed lifted flame.
- In the fuel-lean premixed flame, based on conditional sampling of the intensity of the OH×HCHO fluorescence and the local dilatation rate, it is concluded that the inner secondary vortex structure promotes combustion both by locally enlarging the flame front and by enhancing the heat and mass exchange between the combustion products inside the recirculation zone and the fresh mixture.
- In the partially premixed lifted flame, the conditionally sampled dilatation rate (i.e., the divergence of the velocity field) indicates that the outer helical secondary vortex promotes combustion via locally enhanced entrainment of the surrounding air by the fuel-rich jet. This conclusion is in agreement with our previous study of a lifted swirling propane flame under periodic modulation of the flow rate [30].
- In general, for the typical types of flames from swirl burners (V-type lean premixed and M-type partially premixed lifted flames) it is demonstrated that the helical vortex structures are coupled with the local regions of elevated heat release rates. The evidence from the phase-averaged HCHO×OH PLIF signal and local dilatation rate that despite the observed events of local flame extinction, on average the inner spiraling vortex structure promotes stabilization of the lean premixed flame via locally enlarged flame surface and enhanced heat and mass exchange between the combustion products and fresh mixture. The phase averaging indicates that this helical region of the elevated heat release rotates around the burner axis simultaneously with the precessing spiraling vortex structure. This experimental finding is important for better understanding of sources of thermoacoustic pulsations in swirling flames.

Appendix A: Swirl rate for the non-reacting flow

Figure A1 shows the profiles of the mean velocity and the second-order statistical moments of the velocity fluctuations in the vicinity of the nozzle exit for a non-reacting jet. The axial velocity is negative on the jet axis, indicating that the recirculation zone penetrates inside the nozzle. The magnitude of the angular velocity appears to be close to the maximal values of the axial velocity profile. Based on the mean velocity and second-order moments, the time-averaged flux M_y of the axial momentum through a transversal cross-section of the jet and the flux M_Ω of the angular momentum can be estimated to evaluate the swirl rate Sw . These values are shown in Figure A2 for different distances from the nozzle exit. For the considered measurement plane for $x > 0$ the radial and azimuthal velocity components are evaluated as $u_r = u_x$ and $u_\theta = -u_z$, respectively, and the radial coordinate r coincides x . On average, Sw appears to be close to 1.2 with the highest deviation in the central recirculation zone.

$$M_y = \pi\rho \int_{-\infty}^{+\infty} r \left(U_y^2 + \langle u_y'^2 \rangle + (P - P_\infty) / \rho \right) dr \approx$$

$$\approx \pi\rho \int_{-\infty}^{+\infty} r \left(U_y^2 + \langle u_y'^2 \rangle - \frac{U_\theta^2}{2} - \frac{\langle u_\theta'^2 \rangle + \langle u_r'^2 \rangle}{2} \right) dr,$$

$$M_\Omega(y) = \pi\rho \int_{-\infty}^{+\infty} r^2 \left(U_y U_\theta + \langle u_y' u_\theta' \rangle \right) dr, \quad Sw = \frac{M_\Omega}{M_y} \frac{2}{d}$$

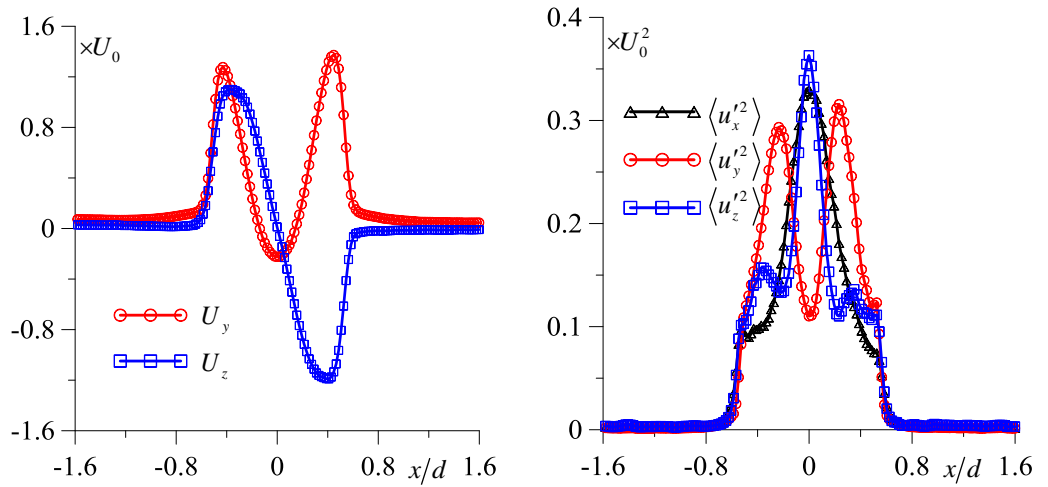


Fig. A1. Distribution of the mean velocity and deviations of the velocity fluctuations near the nozzle exit ($y/d \approx 0.1$) of the high-swirl jet.

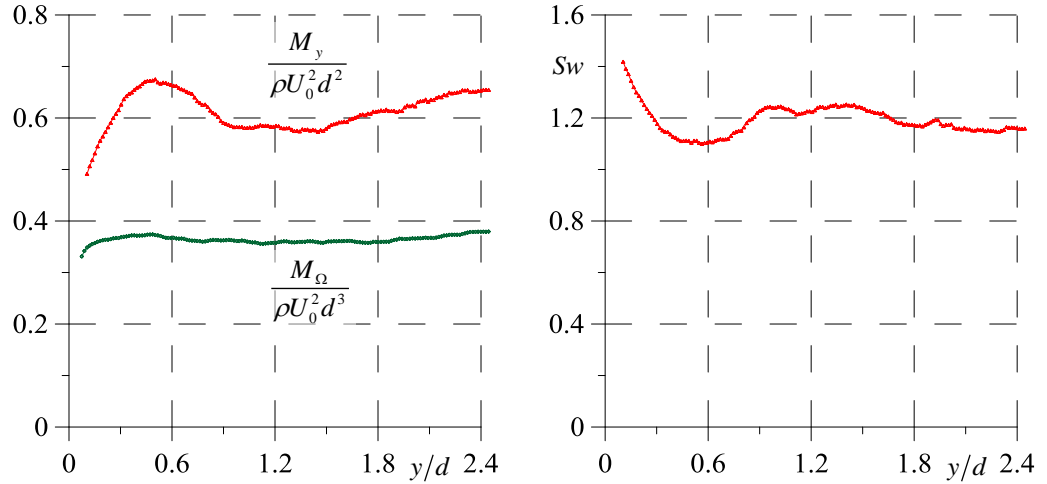


Fig. A2. Axial fluxes of the jet's angular and axial momenta and the swirl rate along the high-swirl jet.

Appendix B: Effect of spatial resolution

Figures B1 and B2 demonstrate the effect of spatial averaging on the PLIF data, where Δ_{PLIF} is the size of the averaging window. The data for the resolution used in the present paper, $\Delta_{\text{PLIF}} = \Delta_{\text{PIV}} = 0.57$ mm, are compared with windows sizes that are two and four times smaller and larger. As seen from the profiles, a decrease in the spatial resolution (i.e., increase in Δ_{PLIF}) results in a smoothing effect, whereas for smaller Δ the profiles remain similar. This means that for $\Delta_{\text{PLIF}} = 0.57$ mm the reached resolution is already maximal due to the fixed laser sheet thickness. This example shows that the selected Δ_{PLIF} in the present paper provides an optimal trade-off between the maximal spatial resolution and the signal-to-noise ratio due to the spatial smoothing.

For the present examples, a Canny filter was not used to remove the isolated bright dots, which are presumably caused by the fluorescence of the TiO_2 tracer particles when illuminated by a UV laser [68]. In the cold flow region inside the cone, where concentration of the tracer particles was the highest, the spatially averaged intensity is below 40 counts. Behind the flame front, the bright dots of the fluorescent light are visible. The spatial-averaged intensity is approximately 120 counts. This value appears to be considerably lower than the 1800 counts at the flame front, where the signal should be the sum of the HCHO and TiO_2 fluorescence. Thus, the contribution of the tracer particles to the PLIF intensity can be evaluated as 6.5%, which is very small (note that the Canny filter was not used during this test).

Additional tests have been performed for turbulent swirling flames when the PIV system was not used and the TiO_2 tracer particles were not added to the flow. No significant difference was observed between the images.

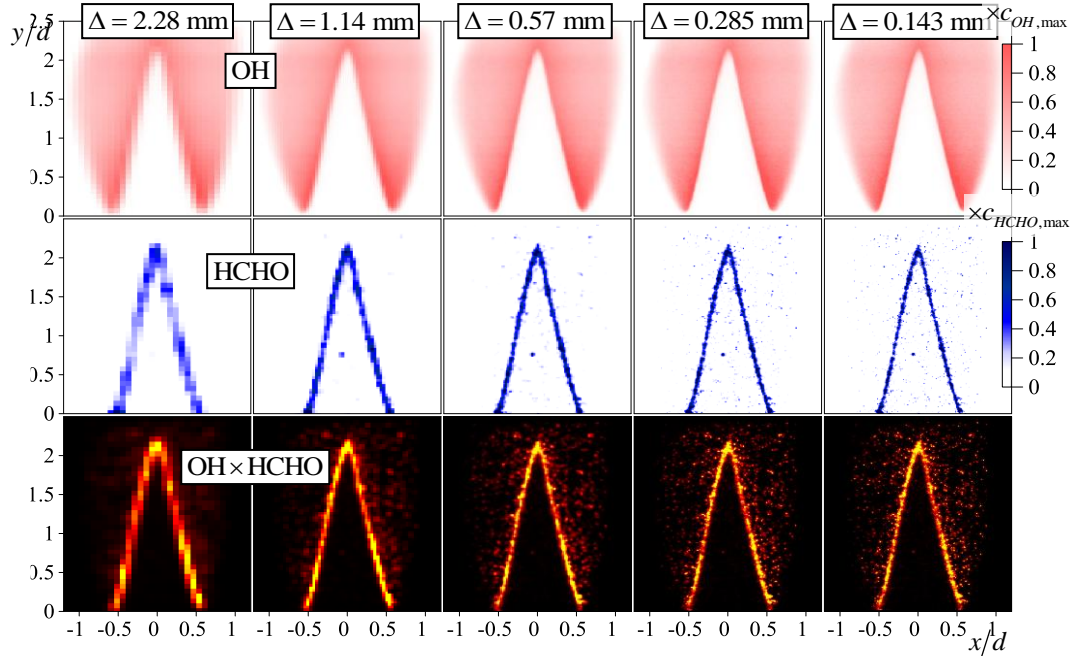


Fig. B1. Effect of the spatial resolution (Δ is the window size) on the instantaneous snapshots of the PLIF data for the Bunsen flame. $c_{HCHO,max} = 1830$, $c_{OH,max} = 31800$.

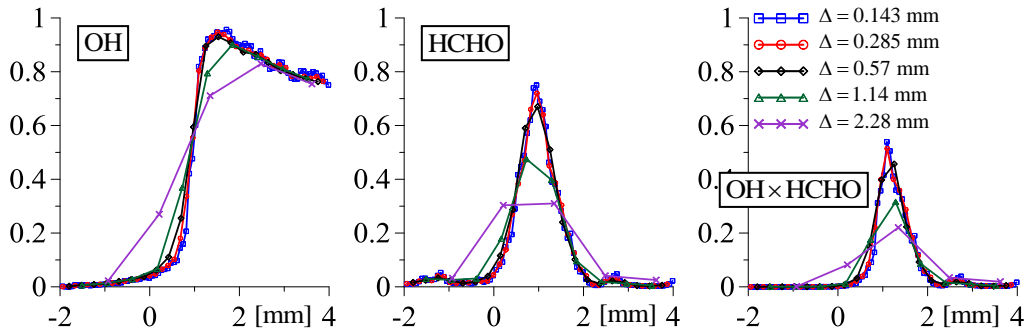


Fig. B2. Profiles of the PLIF intensity across the front of the Bunsen flame for various spatial resolutions.

Acknowledgements. The research here presented was supported by the Russian Science Foundation (Grant No. 16-19-10566). The authors are grateful to Egor Palkin for assistance in data processing and Dmitry Sharaborin for help during PIV/PLIF measurements.

References:

[1] Gupta, A.K., Lilley, D.G., Syred, N.: Swirl Flows. Abacus Press, Kent, England (1984).

- [2] Dellenback, P.A., Metzger, D.E., Neitzel, G.P.: Measurements in turbulent swirling flow through an abrupt axisymmetric expansion. *AIAA J.* 26(6), 669-681 (1988).
- [3] Alekseenko, S.V., Kuibin, P.A., Okulov, V.L.: *Theory of Concentrated Vortices: An Introduction*. Springer (2007).
- [4] Chanaud, R.C.: Observations of oscillatory motion in certain swirling flows. *J. Fluid Mech.* 21(1), 111-127 (1965).
- [5] Cassidy, J.J., Falvey, H.T.: Observations of unsteady flow arising after vortex breakdown. *J. Fluid Mech.* 41(4), 727-736 (1970).
- [6] Leibovich, S.: The structure of vortex breakdown. *Annu. Rev. Fluid Mech.* 10(1), 221-246 (1978).
- [7] Spall, R.E.: Transition from spiral to bubble-type vortex breakdown. *Phys. Fluids* 8(5), 1330-1332 (1996).
- [8] Lucca-Negro, O., O'Doherty, T.: Vortex breakdown: a review. *Prog. Energy Combust. Sci.* 27(4), 431-522 (2001).
- [9] Keck, O., Meier, W., Stricker, W., Aigner, M.: Establishment of a confined swirling natural gas/air flame as a standard flame: Temperature and species distributions from laser Raman measurements. *Combust. Sci. Technol.* 174(8), 117-151 (2002).
- [10] Anacleto, P.M., Fernandes, E.C., Heitor, M.V., Shtork, S.I.: Swirl flow structure and flame characteristics in a model lean premixed combustor. *Combust. Sci. Technol.*, 175(8), 1369-1388 (2003).
- [11] Giezendanner-Thoben, R., Meier, U., Meier, W., Heinze, J., Aigner, M.: Phase-locked two-line OH planar laser-induced fluorescence thermometry in a pulsating gas turbine model combustor at atmospheric pressure. *Appl. Opti.* 44(31), 6565-6577 (2005).
- [12] Weigand, P., Meier, W., Duan, X. R., Stricker, W., Aigner, M.: Investigations of swirl flames in a gas turbine model combustor: I. Flow field, structures, temperature, and species distributions. *Combust. Flame*, 144(1-2), 205-224 (2006).
- [13] Syred, N., Chigier, N.A., Beér, J.M.: Flame stabilization in recirculation zones of jets with swirl. *Proc. Combust. Inst.* 13(1), 617-624 (1971).
- [14] Syred, N., Beer, J.M.: Combustion in swirling flows: a review. *Combust. Flame* 23(2), 143-201 (1974).
- [15] Cheng, R.K.: Velocity and scalar characteristics of premixed turbulent flames stabilized by weak swirl. *Combust. Flame*. 101(1-2): 1-14 (1995).
- [16] Johnson, M.R., Littlejohn, D., Nazeer, W.A., Smith, K.O., Cheng, R.K.: A comparison of the flowfields and emissions of high-swirl injectors and low-swirl injectors for lean premixed gas turbines. *Proc. Combust. Inst.* 30(2), 2867-2874 (2005).
- [17] Cheng, R.K.: Low swirl combustion. *The Gas Turbine Handbook* (Ed.: R. Dennis), Department of Energy, Washington, DC, 241-255 (2006).
- [18] Syred, N.: A review of oscillation mechanisms and the role of the precessing vortex core (PVC) in swirl combustion systems. *Prog. Energy Combust. Sci.* 32(2), 93-161 (2006).
- [19] Sarpkaya, T.: Vortex-induced oscillations: a selective review. *J. Appl. Mech.* 46(2), 241-258 (1979).

- [20] Sreenivasan, K.R., Strykowski, P.J.: An instability associated with a sudden expansion in a pipe flow. *Phys. Fluids* 26(10), 2766–2768 (1983).
- [21] Akhmetov, D.G., Nikulin, V.V., Petrov, V.M.: Experimental study of self-oscillations developing in a swirling-jet flow. *Fluid Dynamics* 39(3), 406–413 (2004).
- [22] Fernandes, E.C., Heitor, M.V., Shtork, S.I.: An analysis of unsteady highly turbulent swirling flow in a model vortex combustor. *Exp. Fluids* 40(2), 177–187 (2005).
- [23] Litvinov, I.V., Shtork, S.I., Kuibin, P.A., Alekseenko, S.V., Hanjalic, K.: Experimental study and analytical reconstruction of precessing vortex in a tangential swirler. *Int. J. Heat Fluid Flow*, 42, 251–264 (2013).
- [24] Cafiero, G., Ceglia, G., Discetti, S., Ianiro, A., Astarita, T., Cardone, G.: On the three-dimensional precessing jet flow past a sudden expansion. *Exp. Fluids*, 55(2), 1677 (2014).
- [25] Terhaar, S., Reichel, T. G., Schrodinger, C., Rukes, L., Paschereit, C.O., Oberleithner, K.: Vortex breakdown types and global modes in swirling combustor flows with axial air injection. *J. Propuls. Power* 31(1), 219–229 (2015).
- [26] Percin, M., Vanierschot, M., van Oudheusden, B.W.: Analysis of the pressure fields in a swirling annular jet flow. *Exp. Fluids* 58(12), 166 (2017).
- [27] Alekseenko, S.V., Abdurakipov, S.S., Hrebtov, M.Y., Tokarev, M.P., Dulin, V.M., Markovich, D.M.: Coherent structures in the near-field of swirling turbulent jets: A tomographic PIV study. *Int. J. Heat Fluid Flow* 70, 363–379 (2018).
- [28] Cala, C.E., Fernandes, E.C., Heitor, M.V., Shtork, S.I.: Coherent structures in unsteady swirling jet flow. *Exp. Fluids* 40(2), 267–276 (2006).
- [29] Oberleithner, K., Sieber, M., Nayeri, C.N., Paschereit, C.O., Petz, C., Hege, H.-C., Noack, B.R., Wygnanski, I.: Three-dimensional coherent structures in a swirling jet undergoing vortex breakdown: Stability analysis and empirical mode construction. *J. Fluid Mech.* 679, 383–414 (2011).
- [30] Alekseenko, S.V., Dulin, V.M., Kozorezov, Y.S., Markovich, D.M.: Effect of high-amplitude forcing on turbulent combustion intensity and vortex core precession in a strongly swirling lifted propane/air flame. *Combust. Sci. Technol.* 184(10–11), 1862–1890 (2012).
- [31] Martinelli, F., Cozzi, F., Coghe, A.: Phase-locked analysis of velocity fluctuations in a turbulent free swirling jet after vortex breakdown. *Exp. Fluids* 53(2), 437–449 (2012).
- [32] Sirovich, L.: Turbulence and the dynamics of coherent structures. I. Coherent structures. *Quart. Appl. Math.* 45(3), 561–571 (1987).
- [33] Alekseenko, S.V., Dulin, V.M., Tokarev, M.P., Markovich, D.M.: A swirling jet with vortex breakdown: three-dimensional coherent structures. *Thermophys. Aeromech.* 23(2), 301–304 (2016).
- [34] Ceglia, G., Discetti, S., Ianiro, A., Michaelis, D., Astarita, T., Cardone, G.: Three-dimensional organization of the flow structure in a non-reactive model aero engine lean burn injection system. *Exp. Therm. Fluid Sci.* 52, 164–173 (2014)
- [35] Markovich, D.M., Dulin, V.M., Abdurakipov, S.S., Kozinkin, L.A., Tokarev, M.P., Hanjalić, K.: Helical modes in low- and high-swirl jets measured by tomographic PIV. *J. Turbul.* 17(7), 678–698 (2016).

- [36] Syred, N., Beer, J.M.: The damping of precessing vortex cores by combustion in swirl generators. *Astronautica Acta* 17(4-5), 783–801 (1972).
- [37] Syred, N., Fick, W., O'Doherty, T., Griffiths, A.J.: The effect of the precessing vortex core on combustion in a swirl burner. *Combust. Sci. Technol.* 125(1-6), 139–157 (1997).
- [38] Huang, Y., Yang, V.: Dynamics and stability of lean-premixed swirl-stabilized combustion. *Prog. Energy Combust. Sci.* 35(4), 293-364 (2009).
- [39] Schneider, C., Dreizler, A., Janicka, J.: Fluid dynamical analysis of atmospheric reacting and isothermal swirling flows. *Flow, Turbul. Combust.* 74(3), 103-127 (2005).
- [40] Duwig, C., Fuchs, L.: Large eddy simulation of vortex breakdown/flame interaction. *Phys. Fluids* 19(7), 075103 (2007).
- [41] Janus, B., Dreizler, A., Janicka, J.: Experimental study on stabilization of lifted swirl flames in a model GT combustor. *Flow Turbul. Combust.*, 75(1-4), 293-315 (2005).
- [42] Terhaar, S., Oberleithner, K., Paschereit, C.O.: Key parameters governing the precessing vortex core in reacting flows: An experimental and analytical study. *Proc. Combust. Inst.* 35(3), 3347-3354 (2015).
- [43] Stöhr, M., Sadanandan, R., Meier, W.: Phase-resolved characterization of vortex–flame interaction in a turbulent swirl flame. *Exp. Fluids* 51(4), 1153-1167 (2011).
- [44] Boxx, I., Stöhr, M., Carter, C., Meier, W.: Temporally resolved planar measurements of transient phenomena in a partially premixed swirl flame in a gas turbine model combustor. *Combust. Flame* 157(8), 1510-1525 (2010).
- [45] Stöhr, M., Boxx, I., Carter, C.D., Meier, W.: Experimental study of vortex-flame interaction in a gas turbine model combustor. *Combust. Flame* 159(8), 2636-2649 (2012).
- [46] Boxx, I., Arndt, C. M., Carter, C. D., Meier, W.: High-speed laser diagnostics for the study of flame dynamics in a lean premixed gas turbine model combustor. *Exp. Fluids*, 52(3), 555-567 (2012).
- [47] Huang, Y., Wang, S., Yang, V.: Systematic analysis of lean-premixed swirl-stabilized combustion. *AIAA J.* 44(4) 724-740 (2006).
- [48] Meier, W., Boxx, I., Stöhr, M., Carter, C.D.: Laser-based investigations in gas turbine model combustors. *Exp. Fluids* 49:865-882 (2010).
- [49] Arndt, C.M., Severin, M., Dem, C., Stöhr, M., Steinberg, A.M., Meier, W.: Experimental analysis of thermo-acoustic instabilities in a generic gas turbine combustor by phase-correlated PIV, chemiluminescence, and laser Raman scattering measurements. *Exp. Fluids* 56:69 (2015).
- [50] Giezendanner-Thoben, R., Meier, U., Meier, W., Heinze, J., Aigner, M.: Phase-locked two-line OH planar laser-induced fluorescence thermometry in a pulsating gas turbine model combustor at atmospheric pressure. *Appl. Optics* 44(31), 6565-6577 (2005).
- [51] Steinberg, A.M., Boxx I., Stöhr, M., Meier, W., Carter, C.D.: Effects of flow structure dynamics on thermoacoustic instabilities in swirl-stabilized combustion. *AIAA J.* 50(4) 952-967 (2006).
- [52] Fayoux, A., Zähringer, K., Gicquel, O., Rolon, J.: Experimental and numerical determination of heat release in counterflow premixed laminar flames. *Proc. Combust. Inst.* 30(1), 251-257 (2005).

- [53] Kariuki, J., Dowlut, A., Yuan, R., Balachandran, R., Mastorakos, E.: Heat release imaging in turbulent premixed methane–air flames close to blow-off. *Proc. Combust. Inst.* 35(2), 1443-1450 (2015).
- [54] Mulla, I.A., Dowlut, A., Hussain, T., Nikolaou, Z.M., Chakravarthy, S.R., Swaminathan, N., Balachandran, R.: Heat release rate estimation in laminar premixed flames using laser-induced fluorescence of CH₂O and H-atom. *Combust. Flame* 165, 373-383 (2016).
- [55] Röder, M., Dreier, T., Schulz, C.: Simultaneous measurement of localized heat-release with OH/CH₂O–LIF imaging and spatially integrated OH* chemiluminescence in turbulent swirl flames. *Proc. Combust. Inst.* 34(2), 3549-3556 (2013).
- [56] Alekseenko, S.V., Dulin, V.M., Kozorezov, Y.S., Markovich, D.M., Shtork, S.I., Tokarev, M.P.: Flow structure of swirling turbulent propane flames. *Flow, Turbul. Combust.* 87(4), 569-595 (2011).
- [57] Scarano, F.: Iterative image deformation methods in PIV. *Meas. Sci. Technol.* 13(1), R1–R19 (2002).
- [58] Coudert, S.J.M., Schon, J.P.: Back-projection algorithm with misalignment corrections for 2D3C stereoscopic PIV. *Meas. Sci. Technol.* 12(9), 1371-1381 (2001).
- [59] Luque, J., Crosley, D.: Lifbase: Database and spectral simulation (version 1.5). SRI International Report, MP. 99-009 (1999).
- [60] Brackmann, C., Nygren, J., Bai, X., Li, Z., Bladh, H., Axelsson, B., Denbratt, I., Koopmans, L., Bengtsson, P.-E., Alden, M.: Laser-induced fluorescence of formaldehyde in combustion using third harmonic Nd:YAG laser excitation. *Spectrochim. Acta Part A.* 59, 3347-3356 (2003).
- [61] Kerschen, G., Golinval, J.C., Vakakis, A.F., Bergman, L.A.: The method of proper orthogonal decomposition for dynamical characterization and order reduction of mechanical systems: an overview. *Nonlinear Dyn.* 41(1-3), 147–169 (2005).
- [62] van Oudheusden, B.W., Scarano, F., Van Hinsberg, N.P., Watt, D.W.: Phase-resolved characterization of vortex shedding in the near wake of a square-section cylinder at incidence. *Exp. Fluids* 39(1), 86-98 (2005).
- [63] Legrand, M., Nogueira, J., Lecuona, A., Nauri, S., Rodriguez, P.A.: Atmospheric low swirl burner flow characterization with Stereo-PIV. *Exp. Fluids* 48(5), 901–913 (2010).
- [64] Hussain, A.K.M.F., Reynolds, W.C.: The mechanics of an organized wave in turbulent shear flow. *J. Fluid Mech.* 41(2), 241-258 (1970).
- [65] Antonia, R.A.: Conditional sampling in turbulence measurement. *Annu. Rev. Fluid Mech.* 13(1), 131-156 (1981).
- [66] Mueller, C.J., Driscoll, J.F., Reuss, D.L., Drake, M.C.: Effects of unsteady stretch on the strength of a freely-propagating flame wrinkled by a vortex. *Proc. Combust. Inst.* 26(1), 347-355 (1996).
- [67] Hunt, J.C.R., Wray, A.A., Moin, P.: Eddies, streams, and convergence zones in turbulent flows. Center for Turbulent Research Report CTR-S88, 193–208 (1988).
- [68] Eitel, F., Pareja, J., Johchi, A., Böhm, B., Geyer, D., Dreizler, A.: Temporal evolution of auto-ignition of ethylene and methane jets propagating into a turbulent hot air co-flow vitiated with NO_x. *Combust. Flame* 177: 193-206 (2017).